

Investigating the Impact of Multi-LiDAR Placement on Object Detection for Autonomous Driving

Hanjiang Hu^{1*} Zuxin Liu^{1*} Sharad Chitlangia^{2†} Akhil Agnihotri^{3†} Ding Zhao¹

¹Carnegie Mellon University ²Amazon ³University of Southern California

{hanjianghu,zuxinl,dingzhao}@cmu.edu, chitshar@amazon.com, akhil.agnihotri@usc.edu

Abstract

The past few years have witnessed an increasing interest in improving the perception performance of LiDARs on autonomous vehicles. While most of the existing works focus on developing new deep learning algorithms or model architectures, we study the problem from the physical design perspective, i.e., how different placements of multiple LiDARs influence the learning-based perception. To this end, we introduce an easy-to-compute information-theoretic surrogate metric to quantitatively and fast evaluate LiDAR placement for 3D detection of different types of objects. We also present a new data collection, detection model training and evaluation framework in the realistic CARLA simulator to evaluate disparate multi-LiDAR configurations. Using several prevalent placements inspired by the designs of self-driving companies, we show the correlation between our surrogate metric and object detection performance of different representative algorithms on KITTI through extensive experiments, validating the effectiveness of our LiDAR placement evaluation approach. Our results show that sensor placement is non-negligible in 3D point cloud-based object detection, which will contribute to 5% ~ 10% performance discrepancy in terms of average precision in challenging 3D object detection settings. We believe that this is one of the first studies to quantitatively investigate the influence of LiDAR placement on perception performance.

1. Introduction

LiDAR sensors are becoming the critical 3D sensors for autonomous vehicles (AVs) since they could provide accurate 3D geometry information and precise distance measures under various driving conditions [26]. The point cloud data generated from LiDARs has been used to perform a series of perception tasks, such as object detection and tracking [38, 39, 41], SLAM and localization [27, 51], etc.

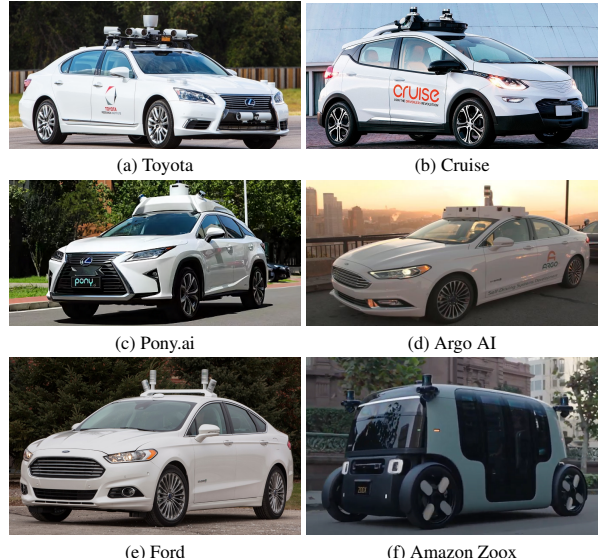


Figure 1. Different multi-LiDAR configurations used in different autonomous vehicles [1–6].

High-quality point cloud data and effective perception algorithms are usually both required to achieve accurate 3D object detection in practice [45]. A number of studies propose to improve the 3D object detection performance for point cloud data by developing novel perception algorithms, which assume that the data is of high quality [15, 22, 39, 41, 46]. However, only a little literature considers the LiDAR perception problem from the viewpoint of data acquisition [21, 25, 28] and LiDAR placement. We believe that this new perspective should be equally crucial for real-world AV applications since improper LiDAR placement may cause poor-quality sensing data, and thus corrupt the perception algorithm and lead to poor performance [11, 21, 24, 25, 30, 45]. In addition, LiDAR is an expensive sensor, so maximizing its utility to save the deployment cost is also important for mass production. Therefore, we aim to investigate the interplay between LiDAR sensor placement and perception performance for AVs. We use placement and configuration interchangeably throughout this paper.

However, it is not easy to evaluate the efficacy of dif-

ferent LiDAR placement layouts based on the perception performance in the real world, which comes with effort-costly and time-consuming full loops of LiDAR deployment, data collection, model training, and performance evaluation. Moreover, as shown in Figure 1, many companies’ self-driving vehicles are equipped with more than 2 LiDARs. As the LiDAR number increases, the cost of LiDAR configuration evaluation and optimization will also increase exponentially. Therefore, it is a crucial but still open problem to accelerate the quantitative evaluation of the LiDAR configurations regarding perception performance with low cost. Thoroughly studying the interplay between LiDAR sensor placement and perception performance is essential to AV perception systems, saving deployment cost and without sacrificing driving safety.

In this paper, we study the perception system from the sensing perspective and focus on investigating the relationship between LiDAR configurations and 3D object detection using our evaluation framework shown in Figure 2. The contributions of this paper are summarized as follows:

- We establish a systematic framework to evaluate the object detection performance of different LiDAR placements and investigate prevalent LiDAR placements inspired by self-driving companies, showing that the placement of LiDARs dramatically influences the performance of object detection up to 10% in challenging 3D detection settings. As far as we are aware, we are one of the first works to quantitatively study the interplay between LiDAR placement and perception performance.
- We propose a novel surrogate metric with maximum information gain (S-MIG) to accelerate the evaluation of LiDAR placement by modeling object distribution through the proposed scalable Probabilistic Occupancy Grids (POG). We show the correlation between the surrogate metric and detection performance, which is theoretically explained via S-MIG and validates its effectiveness for the LiDAR configuration evaluation.
- We contribute an automated multi-LiDAR data collection and detection model evaluation pipeline in the realistic CARLA simulator and conduct extensive experiments with state-of-the-art LiDAR-based 3D object detection algorithms. The results reveal that LiDAR placement plays an important role in the perception system. The code for the framework is available on <https://github.com/HanjiangHu/Multi-LiDAR-Placement-for-3D-Detection>.

2. Related Work

The methods and frameworks proposed in this work revolve around evaluating the LiDAR sensor placement for

point cloud-based 3D object detection in autonomous driving. Although the literature is scarce in this combined area, there has been some research on the 3D object detection and the LiDAR placement optimization topics independently, which we discuss in this section.

LiDAR-based 3D object detection. To keep up with the surge in the LiDAR applications in autonomous vehicles, researchers have tried to develop novel point cloud-based 3D object detection from LiDAR. Over the years, there has also been great progress in grid-based and point-based 3D detection methods for point cloud data. 2D grid-based methods project the point cloud data onto a 2D bird-eye-view (BEV) to generate bounding boxes [14, 22, 23, 43, 43, 49]. Another way to deal with point cloud is to use 3D voxels and 3D CNN, which is also called voxel-based methods [15, 20, 41, 46, 52]. However, these grid-based methods are greatly limited by the kernel size of the 2D or 3D convolution, although the region proposal is pretty accurate with fast detection speed. Point-based methods, on the other hand, directly apply on the raw point cloud based on PointNet series [32–34], which enables them to have flexible perception leading to robust point cloud learning [31, 44, 47, 48]. More receptive fields bring about higher computation costs compared to grid-based methods. Recent work [37, 38] combine voxel-based and point-based methods together to efficiently learn features from raw point cloud data, leading to impressive results on KITTI dataset [19]. To evaluate the influence of point cloud of LiDAR configuration, we use some representative voxel-based and point-based methods [42] in Section 4. The majority of the detection methods mentioned above are well-designed and evaluated on high-quality point cloud datasets, but do not consider the influence of the LiDAR sensing system.

LiDAR placement for autonomous vehicles. One of the critical factors for autonomous vehicles is the perception and sensing ability. With this respect, LiDARs have been widely used because of their high real-time precision and their ability to extract rich information from the environment [19, 29, 51]. However, the perception ability of the LiDAR is sensitive to its placement [17, 50], it is critical to developing a scheme that minimizes the uncertainty among all its possible placements. To this extent, Dybedal *et al.* [18] proposed to find the optimal placement of 3D sensors using a Mixed Integer Linear Programming approach, which is not scalable to AVs because of the large number of variables involved. Rahimian *et al.* [36] developed a dynamic occlusion-based optimal placement routine for 3D motion capture systems, but do not consider variable number of sensors during its optimization routine.

There have also been some prominent advances to optimize the placement of multiple LiDARs for AV while considering the perception performance. Mou *et al.* [30] formulated a min-max optimization problem for LiDAR

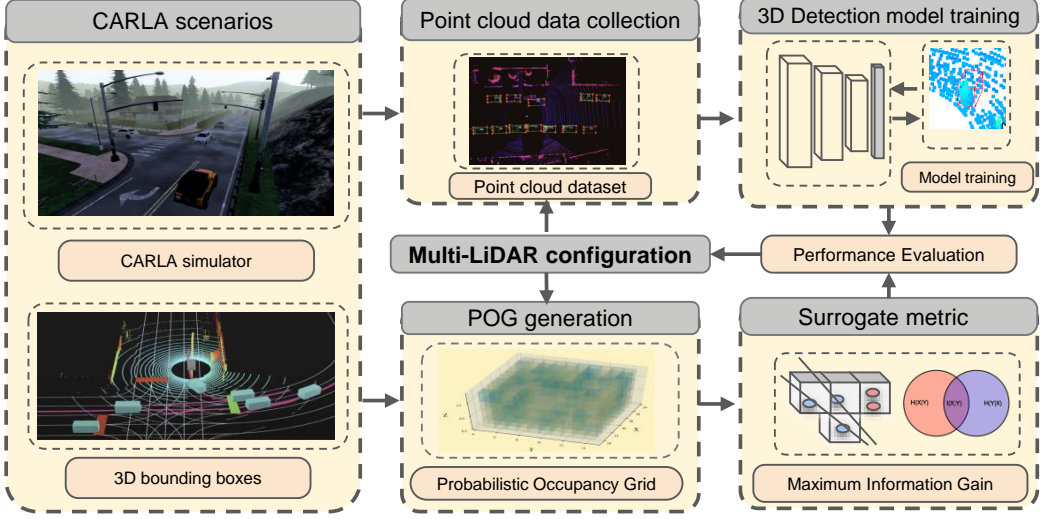


Figure 2. Evaluation framework overview.

placement with a cylinder-based cost function proxy to consider the worst non-detectable inscribed spheres formed by the intersection of different laser beams. Liu *et al.* [25] improved the previous work by using an intuitive volume to surface area (VSA) ratio metric and a black-box heuristic-based optimization method to find the optimal LiDAR placement. These methods assume a uniformly weighted region around the AV to minimize the maximum non-detectable area. They do not explicitly reveal the relation between the LiDAR placement and the perception performance. The closest research to ours is Ma *et al.* [28], which proposed the perception entropy metric for multiple sensor configuration evaluation. Although they use conditional entropy to measure the sensor perception, they rely on empirical assumptions from KITTI dataset in the formulation of perception entropy, which weakens the generalizability to other scenes. We formulate the problem under a full probabilistic framework using a data-driven surrogate metric with a ray-tracing acceleration approach to overcome these limitations.

3. Methodology

To avoid the huge effort of data collection and complicated analysis of learning-based detection for evaluating each multi-LiDAR placement, in this section, we introduce the methodology to efficiently evaluate LiDAR sensor placement for perception performance based on information theory. The problem of LiDAR placement evaluation is formulated and related definitions of Region of Interest (ROI) and Probabilistic Occupancy Grid (POG) are presented. Finally, we describe how to compute the probabilistic surrogate metric for fast LiDAR configuration evaluation.

3.1. Problem Formulation

We begin this section by defining the LiDAR perception model and the ROI, which form the basis of our LiDAR configuration evaluation problem. As shown in Figure 3, we model a LiDAR sensor as a collection of multiple beams. Each beam owns a pitch angle to the XY plane and rotates at a uniform speed along the positive Z axis. As each beam completes one rotation, it forms a conical surface area, and we assume its perception to be all points in this area. Thus, the total perception of a LiDAR is the union of all these conical areas formed by the rotation of its beams in the ROI, which we will describe next.

Similar to previous work [25] and [30], we define the ROI to be the space where we keep track of objects to be detected. To account for LiDAR's limited range of detection, we denote the cuboid size of the ROI to be $[l, w, h]$ for length l along the x -axis, width w along y -axis and height h along the z -axis in the XYZ coordinate system, as shown in Figure 4. The size of ROI is mainly determined by the distribution of target objects (Car, Truck, Cyclist, *etc.*) in the scenario. We then discretize the ROI into voxels with a fixed resolution δ to represent ROI as a collection of voxels,

$$\mathcal{V} = \{v_1, v_2, \dots, v_M\}, M = \frac{l}{\delta} \times \frac{w}{\delta} \times \frac{h}{\delta} \quad (1)$$

The ROI provides us with a fixed perception field around the LiDAR, from which LiDAR beams accumulate most sensing information for the following perception task.

Therefore, for the LiDAR-based 3D object detection task, we only focus on the objects within ROI for each point cloud frame when calculating the perception metrics. Then, the problem of LiDAR placement evaluation is formulated as comparing the object detection performance given Li-

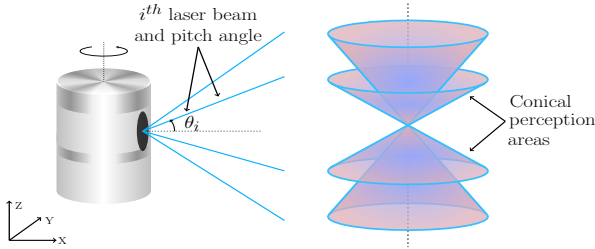


Figure 3. Schematic showing a LiDAR sensor forming perception cones in the ROI to collect point cloud data.

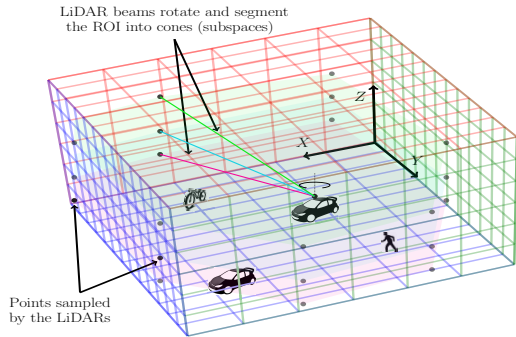


Figure 4. LiDAR sensor mounted on an AV samples object voxels according to 3D bounding boxes from the ROI and generate the POG to evaluate detection performance.

DAR configuration candidate using common point cloud-based 3D object detection algorithms and their metrics [19]. However, directly using 3D object detection metrics to evaluate the LiDAR placement in the real world is inaccurate and extremely inefficient, as it is impossible to make all the scenarios and objects identical to collect point cloud data fairly for evaluated LiDAR configuration candidate in the practical application. Besides, it may take days for each evaluation procedure to collect new data and train the detection models based on new LiDAR placement to get the final detection metrics. Therefore, we propose a new surrogate metric to accelerate the LiDAR placement evaluation procedure based on the Probabilistic Occupancy Grid.

3.2. Probabilistic Occupancy Grid

Since we consider the 3D object detection in ROI among all the frames, intuitively, the LiDAR configurations covering more objects will perform better in the object detection task. To this end, we propose to model the joint distribution of voxels in ROI as Probabilistic Occupancy Grid (POG) by estimating the probability of each voxel to be occupied. For each object of interest, like car, truck and cyclist, the POG is defined as the joint probability of occupied voxels by 3D bounding boxes (BBoxes) among all the frames from M voxels in ROI. Similarly, let the LiDAR configuration be random variable C , given LiDAR configuration $C = C_0$, conditional POG can represent the conditional joint distri-

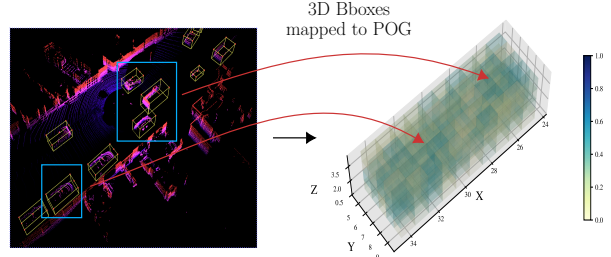


Figure 5. Schematic showing how 3D bounding boxes (Bboxes) are mapped to the ROI to generate a POG. Each cube in the POG has a probability given by Equation 4.

bution of occupied voxels given the specific LiDAR configuration with the assumption of conditional independence.

$$p_{POG} = p(v_1, v_2, \dots, v_M) \quad (2)$$

$$p_{POG|C=C_0} = p(v_1, v_2, \dots, v_M | C = C_0) \quad (3)$$

where $v_i \sim p_{\mathcal{V}}$. To make the notation compact and easy to read, we denote the occupied voxel random variable $v_i | C = C_0$ as $v_i^{C_0}$ and denote the conditional distribution $p_{\mathcal{V}|C=C_0}$ as $p_{\mathcal{V}|C_0}$, so we have $v_i^{C_0} \sim p_{\mathcal{V}|C_0}$.

To estimate POG from samples, given a dataset of the ground truth of BBoxes $\mathcal{Y}_T = \{y_1, y_2, \dots, y_T\}$, where T represents the number of ground truth frames. Each frame $y_t (t \in \{1, \dots, T\})$ contains $N^{(t)}$ 3D BBoxes of the target object $\{b_1^{(t)}, b_2^{(t)}, \dots, b_{N^{(t)}}^{(t)}\}$ within ROI of the ego-vehicle, and each BBox is parameterized by its center coordinates, size (length, width, height), and yaw orientation. For each voxel coordinate $v_i = (x_i, y_i, z_i) \in \mathcal{V}$, we denote $v_i \in y_t$ if v_i is within any of the bounding boxes $\{b_1^{(t)}, b_2^{(t)}, \dots, b_{N^{(t)}}^{(t)}\}$. Then, for each voxel $v_i \in \mathcal{V}$ from ROI, we estimate its probability to be occupied among all the T frames as,

$$\hat{p}(v_i) = \frac{\sum_{t=1}^T \mathbb{1}(v_i \in y_t)}{T}, i = 1, 2, \dots, M \quad (4)$$

$$v_i \in y_t := \exists b^{(t)} \in y_t, s.t. v_i \in b^{(t)} \quad (5)$$

where $\mathbb{1}(\cdot)$ is an indicator function and M is the number of voxels in ROI. The POG can then be estimated by the joint probability of all occupied voxels in ROI. Since the presence of an object in one voxel does not imply presence in other voxels among all the frames in ROI, we could treat these voxels as independent and identically distributed random variables and calculate the joint distribution over all voxels in the set \mathcal{V} as,

$$\hat{p}_{POG} = \hat{p}(v_1, \dots, v_M) = \prod_{i=1, \hat{p}(v_i) \neq 0}^M \hat{p}(v_i) \quad (6)$$

where M is the total number of non-zero voxels in ROI. One such example of the POG of car is shown in Figure 5. Note

that notations of \hat{p} with $\hat{}$ are the estimated distribution from observed samples, while notations of p without $\hat{}$ are the unknown non-random true distribution to be estimated.

For a particular LiDAR configuration $C = C_0$, we employ ray tracing by Bresenham’s Line Algorithm [10] (denoted as $Bresenham(\mathcal{V}, C_0)$) to find all the voxels which intersect with the perception field (ROI) of that LiDAR. We denote the set of these beam-intersected voxels as,

$$\mathcal{V}|C_0 = Bresenham(\mathcal{V}, C_0) = \{v_1^{C_0}, \dots, v_M^{C_0}\} \quad (7)$$

where the discretized non-zero voxels from LiDAR beams give the perception range of LiDAR configuration C_0 .

The conditional probability of occupied voxels among all frames in ROI given the LiDAR configuration C_0 can represent the conditional distribution from which LiDAR can get sensing information of the target object. Similar to Equation 6, the conditional POG given LiDAR configuration C_0 can be estimated as,

$$\hat{p}_{POG|C_0} = \hat{p}(v_1^{C_0}, \dots, v_M^{C_0}) = \prod_{i=1, \hat{p}(v_i^{C_0}) \neq 0}^M \hat{p}(v_i^{C_0}) \quad (8)$$

From the perspective for density estimation to find POG, combine Equation 2, 3, 6 and 8, the true POG and conditional POG given configuration C_0 can be estimated as,

$$p_{POG} = \hat{p}_{POG}, p_{POG|C=C_0} = \hat{p}_{POG|C_0} \quad (9)$$

3.3. Probabilistic Surrogate Metric

In this section, we derive our surrogate metric based on information theory using the POG $p(v_1, \dots, v_M)$ and conditional POG $p(v_1, \dots, v_M | C = C_0)$ given LiDAR configuration C_0 , evaluating how well the LiDAR placement can sense objects’ location in ROI.

To maximize the perception capability, one intuitive way is to reduce the uncertainty of the joint distribution of voxels given specific LiDAR configuration. The total entropy of POG (**POG Entropy**) is only determined by the scenarios with bounding boxes.

$$H_{POG} = H(\mathcal{V}) = \mathbb{E}_{v_i \sim p_{\mathcal{V}}} \sum_{i=1}^M \hat{H}(v_i) \quad (10)$$

Mutual information (MI) of two random variables can represent uncertainty reduction given the condition. In this case, we want to evaluate the information gain (**IG**) of voxels occupied by target objects given the LiDAR configuration candidate. Our insight is that the more IG the LiDAR configuration has, the more information it will contain so the more uncertainty it will reduce. With $p(C = C_0) = 1$,

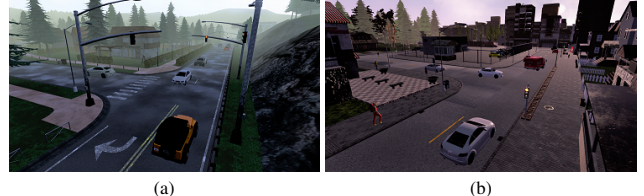


Figure 6. Realistic simulation environments in CARLA.

$$IG_{\mathcal{V}, C_0} = H(\mathcal{V}) - H(\mathcal{V}|C_0) = H(\mathcal{V}) + S_{MIG} \quad (11)$$

$$S_{MIG} = -H(\mathcal{V}|C_0) = -\mathbb{E}_{v_i^{C_0} \sim p_{\mathcal{V}|C_0}} \sum_{i=1}^M \hat{H}(v_i^{C_0}) \quad (12)$$

where we introduce the maximum information gain-based surrogate metric **S-MIG**, ignoring the total entropy $H(\mathcal{V})$ which is a constant given POG and the same for different LiDAR configurations. The entropy of each voxel can be found below.

$$\hat{H}(v_i) = -\hat{p}(v_i) \log \hat{p}(v_i) - (1 - \hat{p}(v_i)) \log(1 - \hat{p}(v_i))$$

4. Experiments

This section aims to address two questions: 1) Does LiDAR placement influence the final perception performance? 2) How can we quantify and evaluate the detection performance of different LiDAR configurations using our easy-to-compute probabilistic surrogate metric? To answer these questions, we conduct extensive experiments in a realistic self-driving simulator — CARLA [16]. Due to the requirement of fairly evaluating different LiDAR placements with all other environmental factors fixed, such as the ego-vehicle’s and surrounding objects’ trajectories, we choose to use realistic simulation scenarios in CARLA (Figure 6), instead of a public real-world dataset.

4.1. Experimental Setup

Given CARLA scenarios and the target object, we obtain the POG based on the bounding box labels and calculate the surrogate metric S-MIG for every LiDAR placement. For each evaluated LiDAR configuration candidate, we first collect point cloud data in CARLA, then train and test all the object detection models using the collected data. Finally, we correlate the surrogate metric and the 3D detection performance, and the results explain the LiDAR performance variance from the information theory perspective,

CARLA simulator. We use CARLA as the simulation platform to collect data and evaluate our method. CARLA is a high-definition open-source simulator for autonomous driving research [12, 13] that offers flexible scenario setups and sensor configurations. CARLA provides realistic rendering and physics simulation based on Unreal Engine 4. Furthermore, the LiDAR sensor could generate accurate point cloud data and could be easily config-

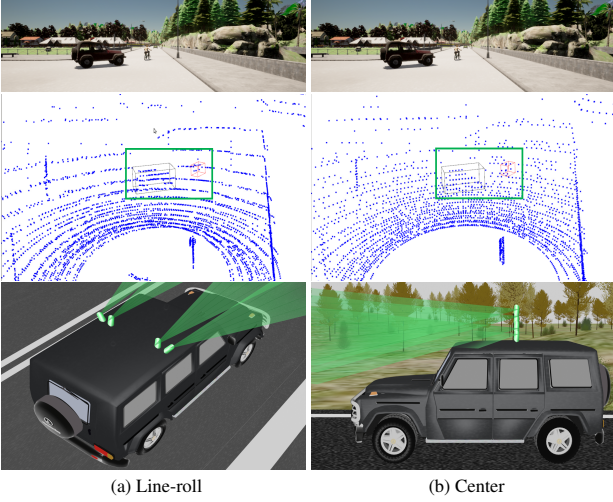


Figure 7. Point cloud data collected from different LiDAR configurations under the same scenarios with car (in black 3D bounding box) and cyclist (in red 3D bounding box).

ured with customized placement. We use CARLA’s in-built ScenarioRunner module to simulate realistic traffic scenarios, only changing LiDAR configurations for all the experiments. We collect data in Town 1, 3, 4, 6 and each town contains 8 manually recorded routes. For Sparse, Medium and Dense scenarios, we spawn 40, 800, 120 Vehicles (including cars, motorcycles, trucks, cyclists, etc.) in each town and the default density is Medium.

Data format. The collected dataset for each LiDAR configuration contains about 45000 point cloud frames with 3D bound boxes of normal-size vehicles as Car (including Sedan, Pickup Truck, SUV, etc.) and other abnormal-size vehicles as Van and Cyclist (including Box Truck, Cyclist, Motorcycles, etc.). We use all collected bounding boxes to calculate POG for each object type and estimate the joint distribution of voxels in ROI. We use about 10% fixed frames as the test set and the remaining data as the training set in all the experiments. The point clouds from different LiDARs are aggregated and transformed to the reference frame of the ego-vehicle for computational convenience. We make the data format consistent with KITTI 3D object detection benchmark [19]. To calculate ROI and POG efficiently for each target object, we customize the size of ROI to be $l = 80m, w = 40m, h = 4m$ for CARLA scenario. Following the KITTI format, we use the half front view of point cloud range (40m in length) when calculating POG and surrogate metric, as well as the 3D detection model training and testing.

3D object detection algorithms and metrics. To fairly compare the object detection performance of different LiDAR configurations, we adopt the recent open-source LiDAR-based 3D object detection framework *OpenPCDet* [42] and fine-tune the KITTI pretrained models of mul-

tiple representative 3D detection algorithms. For voxel-based methods, we use one-stage SECOND [46] and two-stage Voxel RCNN [15]. Also, we use PointRCNN [40] as point-based method and PV-RCNN [37] as the integration of voxel-based and point-based method. Moreover, we also compare the models with 3D Intersection-over-Union (IoU) loss for SECOND [46] and PointRCNN [40]. For detection metrics, we adopt the strictest metrics of Bird-Eye-View (BEV) and 3D detection with average precision across 40% recall under IoU thresholds of 0.70 for Car and 0.50 for Van and Cyclist [19, 42]. We follow the default training hyper-parameters and fine-tune all the KITTI pretrained models for 10 epochs on our training set for the fair comparison between different LiDAR placements. See the supplementary material for more details.

Different LiDAR Placements We evaluate several LiDAR placements as baselines to show the influence on object detection performance. We mainly consider the placement problem of 4 LiDARs and each LiDAR has 20Hz rotation frequency and 90,000 points per frame from the 16 beams. In our experiments, we set beams to be equally distributed in the vertical FOV $[-25.0, 5.0]$ degrees. *Trapezoid* LiDAR configuration is simplified from Toyota’s self-driving cars with 4 LiDARs in the parallel front and back (Figure 1a). *Pyramid* placement is motivated by Cruise and Pony AI (Figure 1b, 1c) including 1 front LiDAR and 3 back ones with a higher one in the middle. *Center* placement is achieved by vertically stacking four LiDARs together at the center of the roof, which is inspired by Argo AI’s autonomous vehicle (Figure 1d). *Line* is motivated by Ford (Figure 1e) and 4 LiDARs are placed in a horizontal line symmetrically. The idea of *Square* comes from Zoox’s self-driving cars (Figure 1f), which places the 4 LiDARs on the 4 roof corners. Furthermore, we investigate the influence of roll rotation on sided LiDARs (*Line-roll*, *Pyramid-roll*). The visualization of baseline placements is shown in Figure 7, and more details of LiDAR placement are presented in the supplementary material.

4.2. Experimental Results and Analysis

To answer the questions raised in Section 4, we demonstrate our evaluation results first to show the influence of different LiDAR placements on 3D object detection, then analyze the relation between detection performance and our surrogate metric in detail. Note that we limit the number of input points per frame to make the detection challenging enough for multi-LiDAR configuration, resulting in lower detection metric values than original KITTI benchmark [19]. See more details in supplementary material.

LiDAR placement influence on 3D object detection. From Table 1 and Figure 8, we present the 3D detection (3D IoU) and bird-eye-view (BEV) performance of representative voxel-based and point-based detection algorithms using

Models	Car-3D (AP_R40@0.70)				Car-BEV (AP_R40@0.70)			
	Center	Line	Pyramid	Trapezoid	Center	Line	Pyramid	Trapezoid
PV-RCNN [37]	52.15	55.50	57.44	57.37	62.64	65.42	65.81	65.54
Voxel RCNN [15]	47.59	50.85	52.61	50.95	57.72	60.84	63.65	61.52
PointRCNN [40]	38.46	48.25	44.28	47.50	51.41	59.14	56.97	59.08
PointRCNN-IoU [40]	38.44	46.86	45.34	47.32	50.56	58.86	56.67	59.04
SECOND [46]	42.89	47.13	46.89	47.53	56.65	59.44	61.75	59.97
SECOND-IoU [46]	44.41	48.60	51.03	49.10	56.98	59.96	62.31	60.28
Models	Van and Cyclist-3D (AP_R40@0.50)				Van and Cyclist-BEV (AP_R40@0.50)			
	Center	Line	Pyramid	Trapezoid	Center	Line	Pyramid	Trapezoid
PV-RCNN [37]	40.09	39.11	40.26	42.85	41.18	41.45	43.09	44.79
Voxel RCNN [15]	33.76	31.60	33.39	33.91	35.40	33.24	35.11	35.54
PointRCNN [40]	31.43	28.00	27.10	30.91	33.86	30.68	30.49	33.75
PointRCNN-IoU [40]	30.75	27.64	26.19	30.54	34.04	30.71	29.30	34.70
SECOND [46]	36.13	32.36	35.32	35.95	38.19	30.68	40.84	40.01
SECOND-IoU [46]	35.61	33.12	34.95	36.51	38.99	36.60	38.31	40.14

Table 1. Comparison of object detection performance under various LiDAR configurations using different algorithms.

point cloud collected with different LiDAR configurations. Note that we use the most rigorous detection metrics in our experiments from [42]. It can be seen that different LiDAR placements clearly influence the detection performance for all the algorithms, varying 10% at most. Moreover, for different target objects, the influence of LiDAR placement is quite different as well. *Pyramid* configuration perform better on Car detection for most algorithms. In contrast, most models trained with data collected with *Trapezoid* placement has higher detection precision for Van and Cyclist object. The reason lies in different POG and point cloud distribution between Car, Van and Cyclist, so the most suitable placement for different target objects is different.

Relation between detection performance and surrogate metric. Now we will show why different LiDAR placements will affect the detection performance using surrogate metric S-MIG. As shown in Figure 8, we illustrate the relation between Car, Van and Cyclist detection performance and S-MIG with all the LiDAR placements using both 3D and BEV average precision metrics. As S-MIG increases, the 3D and BEV detection metrics under all algorithms generally go up for Car, Van and Cyclist detection. The fluctuation in the plots comes from some noise and outliers in data collection and model training, but the increasing trend of detection performance with respect to S-MIG is revealed, which explains the influence of LiDAR placement. More specifically, S-MIG is more smooth in reflecting detection of small objects like cyclists or extremely large objects like box trucks. From Figure 7 we can find that point cloud collected through *Center* is more uniformly distributed so that cyclists get more points to improve the detection performance compared to *Line-roll*, while points on large objects like cars get saturated so the evaluation with S-MIG may be affected.

4.3. Ablation Study and Application Analysis

In this section, we further investigate the influence on placement-detection correlation from some key factors in self-driving, giving examples to evaluate the LiDAR configurations using S-MIG towards potential applications. More details can be found in supplementary material.

Roll angles of sided LiDARs. Orientation of the sided LiDARs are very common, so we investigate the influence of such placement variance in Table 2. It can be found that the placements of *Line-roll* and *Pyramid-roll* with roll angles have worse detection performance as their S-MIG values are lower compared to *Line* and *Pyramid* respectively. The finding is consistent with detection metrics of both 3D and bird-eye-view, which further validates the effectiveness of our surrogate metric and gives an example to fast evaluate the LiDAR placement for object detection.

Density of surrounding road objects. We investigate how scenarios with different object densities affect detection performance and surrogate metric under *Square* placement. Since under scenarios of different object densities, the POG is different and S-MIG cannot be directly used. So the original information gain IG (11) is adopted to involve different POG entropy $H_{POG}(10)$. From Table 3 we can see that the performance gets better when the density of cars increases because the information gain IG gets larger, which shows that our surrogate metric generalizes well to evaluate detection performance under different scenarios.

Potential application analysis. Based on the correlation our surrogate metric and detection performance, the evaluation of different LiDAR placement can be largely accelerated without following the time-consuming procedure: LiDAR installation → massive data collection → model training → evaluation of perception performance. Instead, we

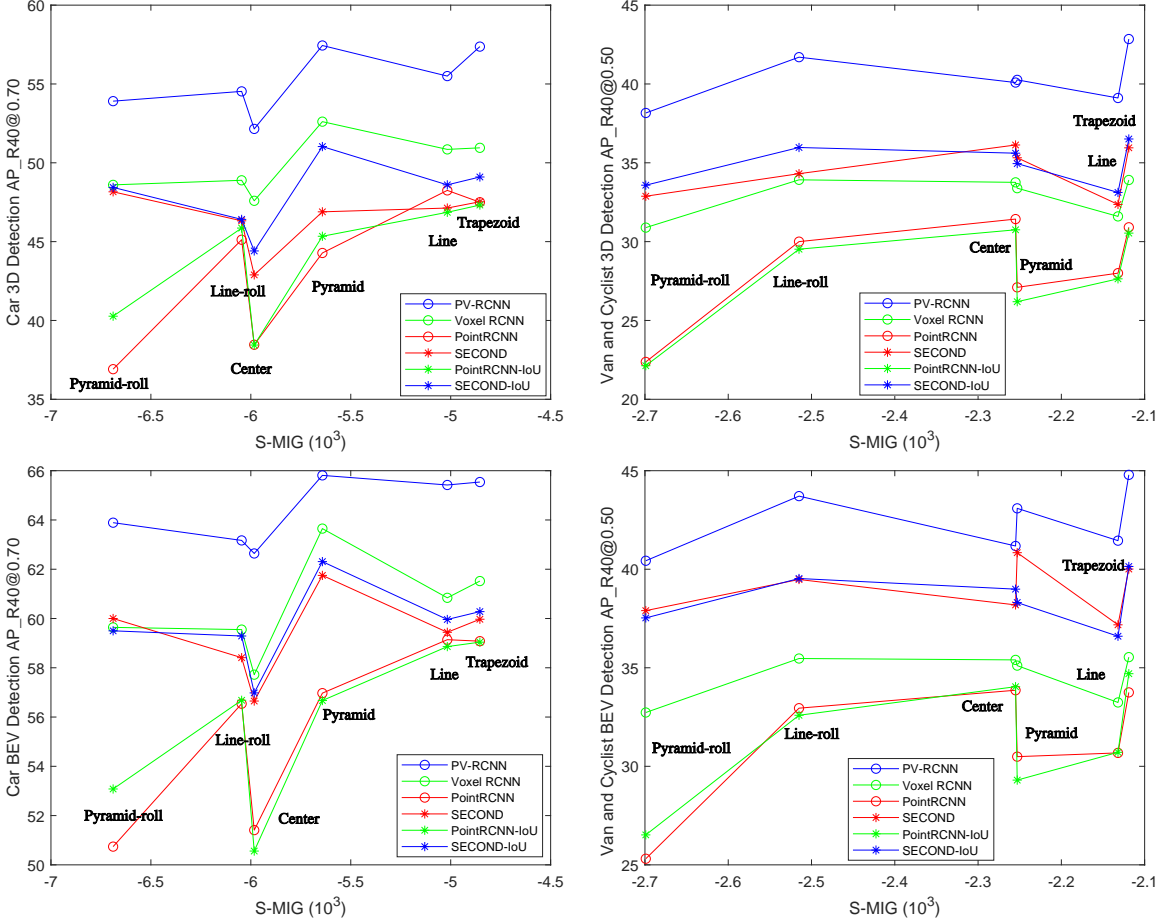


Figure 8. The relationship between Car, Van and Cyclist detection performance and surrogate metric of different LiDAR placements.

3D	PV-RCNN [37]	PointRCNN [40]	S-MIG (10^3)
Line	55.50	48.25	-5.02
Line-roll	54.53	45.12	-6.05
Pyramid	57.44	44.28	-5.64
Pyramid-roll	53.91	36.91	-6.69

BEV	PV-RCNN [37]	PointRCNN [40]	S-MIG (10^3)
Line	65.42	59.14	-5.02
Line-roll	63.17	56.54	-6.05
Pyramid	65.81	56.97	-5.64
Pyramid-roll	63.89	50.74	-6.69

Table 2. Influence of roll rotation of sided LiDARs (as Figure 7a shows) on Car detection performance.

only needs a 3D bounding box dataset of object of interest to generate the POG and evaluate the LiDAR placement, which is fast and economical, and can also be customized in different deployment scenarios.

Moreover, using the proposed surrogate metric, it is easy to optimize the LiDAR placement given the number of LiDARs and their beams under specific scenarios with object of interest. It can maximize the efficacy of the LiDAR sensor and relevant to the AV research community and industry

Density	Dense	Medium	Sparse
PV-RCNN [37]	57.98	56.88	54.48
PointRCNN [40]	48.13	45.46	42.30
SECOND [46]	48.19	47.57	43.96
Voxel RCNN [15]	52.15	51.14	48.15
S-MIG (10^3)	-10.68	-7.63	-6.27
HPOG (10) (10^3)	618.40	496.70	416.96
IG (11) (10^3)	607.072	489.06	410.70

Table 3. Influence of scenarios with different densities of Car on Square 3D detection.

since the current LiDAR placements are more or less intuition driven. Besides, combining with some recent active perception work [7–9, 35], the proposed surrogate metric in this paper could serve as a guidance for those active sensors to focus on important areas around the AV for different scenarios and target objects.

5. Conclusion

This paper investigates the interplay between LiDAR placement and 3D detection performance. We proposed a

novel efficient framework to evaluate multi-LiDAR placement and configuration for AVs. We proposed a data-driven surrogate metric that characterizes the information gain in the conical perception areas, which helps accelerate the LiDAR placement evaluation procedure for LiDAR-based detection performance. Finally, we conducted extensive experiments in CARLA, validating the correlation between perception performance and surrogate metric of LiDAR configuration through representative 3D object detection algorithms. Research in this paper sets a precedent for future work that will optimize the placement of multiple LiDARs and co-design the sensor placement and perception algorithms.

References

- [1] Amazon zoox autonomous vehicle. https://www.youtube.com/watch?v=-PN5_ek0UGk. Accessed: 2021-11-10. 1
- [2] Argo ai autonomous vehicle. <https://www.fleetmanagementweekly.com/argo-ai-receives-1-billion-investment-from-ford-in-the-autonomous-vehicle-race/>. Accessed: 2021-11-10. 1
- [3] Cruise autonomous vehicle. <https://www.wired.com/story/gm-cruise-generation-3-self-driving-car>. Accessed: 2021-11-10. 1
- [4] Ford autonomous vehicle. <https://www.latimes.com/business/autos/la-fi-hy-ford-driverless-car-to-hit-california-roads-20151215-story.html>. Accessed: 2021-11-10. 1
- [5] Pony.ai autonomous vehicle. <https://venturebeat.com/2021/02/07/pony-ai-raises-100-million-more-to-advance-its-autonomous-vehicle-tech/>. Accessed: 2021-11-10. 1
- [6] Toyota autonomous vehicle. <https://techcrunch.com/2017/09/27/toyota-research-institute-self-driving-2-1/>. Accessed: 2021-11-10. 1
- [7] Siddharth Ancha, Gaurav Pathak, Srinivasa G Narasimhan, and David Held. Active safety envelopes using light curtains with probabilistic guarantees. *arXiv preprint arXiv:2107.04000*, 2021. 8
- [8] Siddharth Ancha, Yaadhav Raaj, Peiyun Hu, Srinivasa G Narasimhan, and David Held. Active perception using light curtains for autonomous driving. In *European Conference on Computer Vision*, pages 751–766. Springer, 2020. 8
- [9] Joseph R Bartels, Jian Wang, William Whittaker, Srinivasa G Narasimhan, et al. Agile depth sensing using triangulation light curtains. In *Proceedings of the IEEE/CVF International Conference on Computer Vision*, pages 7900–7908, 2019. 8
- [10] J. E. Bresenham. Algorithm for computer control of a digital plotter. *IBM Systems Journal*, 4(1):25–30, 1965. 5
- [11] Yulong Cao, Chaowei Xiao, Benjamin Cyr, Yimeng Zhou, Won Park, Sara Rampazzi, Qi Alfred Chen, Kevin Fu, and Z Morley Mao. Adversarial sensor attack on lidar-based perception in autonomous driving. In *Proceedings of the 2019 ACM SIGSAC conference on computer and communications security*, pages 2267–2281, 2019. 1
- [12] Dian Chen, Brady Zhou, Vladlen Koltun, and Philipp Krähenbühl. Learning by cheating. In *Conference on Robot Learning*, pages 66–75. PMLR, 2020. 5
- [13] Jianyu Chen, Bodi Yuan, and Masayoshi Tomizuka. Model-free deep reinforcement learning for urban autonomous driving. In *2019 IEEE Intelligent Transportation Systems Conference (ITSC)*, pages 2765–2771. IEEE, 2019. 5
- [14] Xiaozhi Chen, Huimin Ma, Ji Wan, Bo Li, and Tian Xia. Multi-view 3d object detection network for autonomous driving. In *Proceedings of the IEEE conference on Computer Vision and Pattern Recognition*, pages 1907–1915, 2017. 2
- [15] Jiajun Deng, Shaoshuai Shi, Peiwei Li, Wengang Zhou, Yanyong Zhang, and Houqiang Li. Voxel r-cnn: Towards high performance voxel-based 3d object detection. *arXiv preprint arXiv:2012.15712*, 2020. 1, 2, 6, 7, 8
- [16] Alexey Dosovitskiy, German Ros, Felipe Codevilla, Antonio Lopez, and Vladlen Koltun. Carla: An open urban driving simulator. In *Conference on robot learning*, pages 1–16. PMLR, 2017. 5
- [17] Hugh F Durrant-Whyte. Consistent integration and propagation of disparate sensor observations. *The International journal of robotics research*, 6(3):3–24, 1987. 2
- [18] Joacim Dybedal and Geir Hovland. Optimal placement of 3d sensors considering range and field of view. In *2017 IEEE International Conference on Advanced Intelligent Mechatronics (AIM)*, pages 1588–1593. IEEE, 2017. 2
- [19] Andreas Geiger, Philip Lenz, Christoph Stiller, and Raquel Urtasun. Vision meets robotics: The kitti dataset. *The International Journal of Robotics Research*, 32(11):1231–1237, 2013. 2, 4, 6
- [20] Benjamin Graham, Martin Engelcke, and Laurens Van Der Maaten. 3d semantic segmentation with submanifold sparse convolutional networks. In *Proceedings of the IEEE conference on computer vision and pattern recognition*, pages 9224–9232, 2018. 2
- [21] Rohit Ravindranath Kini. Sensor position optimization for multiple lidars in autonomous vehicles, 2020. 1
- [22] Alex H Lang, Sourabh Vora, Holger Caesar, Lubing Zhou, Jiong Yang, and Oscar Beijbom. Pointpillars: Fast encoders for object detection from point clouds. In *Proceedings of the IEEE/CVF Conference on Computer Vision and Pattern Recognition*, pages 12697–12705, 2019. 1, 2
- [23] Ming Liang, Bin Yang, Yun Chen, Rui Hu, and Raquel Urtasun. Multi-task multi-sensor fusion for 3d object detection. In *Proceedings of the IEEE/CVF Conference on Computer Vision and Pattern Recognition*, pages 7345–7353, 2019. 2
- [24] Daniel Liu, Ronald Yu, and Hao Su. Extending adversarial attacks and defenses to deep 3d point cloud classifiers. In *2019 IEEE International Conference on Image Processing (ICIP)*, pages 2279–2283. IEEE, 2019. 1
- [25] Zuxin Liu, Mansur Arief, and Ding Zhao. Where should we place lidars on the autonomous vehicle?—an optimal design approach. In *2019 International Conference on Robotics and Automation (ICRA)*, pages 2793–2799. IEEE, 2019. 1, 3
- [26] Zhe Liu, Shunbo Zhou, Chuanzhe Suo, Peng Yin, Wen Chen, Hesheng Wang, Haoang Li, and Yun-Hui Liu. Lpd-net: 3d point cloud learning for large-scale place recognition and environment analysis. In *Proceedings of the IEEE/CVF International Conference on Computer Vision*, pages 2831–2840, 2019. 1
- [27] Weixin Lu, Guowei Wan, Yao Zhou, Xiangyu Fu, Pengfei Yuan, and Shiyu Song. Deepvcp: An end-to-end deep neural network for point cloud registration. In *Proceedings of the IEEE/CVF International Conference on Computer Vision*, pages 12–21, 2019. 1
- [28] Tao Ma, Zhizheng Liu, and Yikang Li. Perception entropy: A metric for multiple sensors configuration evaluation and design. *arXiv preprint arXiv:2104.06615*, 2021. 1, 3
- [29] Will Maddern, Alex Stewart, Colin McManus, Ben Upcroft, Winston Churchill, and Paul Newman. Illumination invari-

- ant imaging: Applications in robust vision-based localisation, mapping and classification for autonomous vehicles. In *Proceedings of the Visual Place Recognition in Changing Environments Workshop, IEEE International Conference on Robotics and Automation (ICRA), Hong Kong, China*, volume 2, page 3, 2014. [2](#)
- [30] Shenyu Mou, Yan Chang, Wenshuo Wang, and Ding Zhao. An optimal lidar configuration approach for self-driving cars. *arXiv preprint arXiv:1805.07843*, 2018. [1, 2, 3](#)
- [31] Charles R Qi, Or Litany, Kaiming He, and Leonidas J Guibas. Deep hough voting for 3d object detection in point clouds. In *Proceedings of the IEEE/CVF International Conference on Computer Vision*, pages 9277–9286, 2019. [2](#)
- [32] Charles R Qi, Wei Liu, Chenxia Wu, Hao Su, and Leonidas J Guibas. Frustum pointnets for 3d object detection from rgbd data. In *Proceedings of the IEEE conference on computer vision and pattern recognition*, pages 918–927, 2018. [2](#)
- [33] Charles R Qi, Hao Su, Kaichun Mo, and Leonidas J Guibas. Pointnet: Deep learning on point sets for 3d classification and segmentation. In *Proceedings of the IEEE conference on computer vision and pattern recognition*, pages 652–660, 2017. [2](#)
- [34] Charles R Qi, Li Yi, Hao Su, and Leonidas J Guibas. Pointnet++: Deep hierarchical feature learning on point sets in a metric space. *arXiv preprint arXiv:1706.02413*, 2017. [2](#)
- [35] Yaadhav Raaj, Siddharth Ancha, Robert Tamburo, David Held, and Srinivasa G Narasimhan. Exploiting & refining depth distributions with triangulation light curtains. In *Proceedings of the IEEE/CVF Conference on Computer Vision and Pattern Recognition*, pages 7434–7442, 2021. [8](#)
- [36] Pooya Rahimian and Joseph K Kearney. Optimal camera placement for motion capture systems. *IEEE transactions on visualization and computer graphics*, 23(3):1209–1221, 2016. [2](#)
- [37] Shaoshuai Shi, Chaoxu Guo, Li Jiang, Zhe Wang, Jianping Shi, Xiaogang Wang, and Hongsheng Li. Pv-rcnn: Point-voxel feature set abstraction for 3d object detection. In *Proceedings of the IEEE/CVF Conference on Computer Vision and Pattern Recognition*, pages 10529–10538, 2020. [2, 6, 7, 8](#)
- [38] Shaoshuai Shi, Li Jiang, Jiajun Deng, Zhe Wang, Chaoxu Guo, Jianping Shi, Xiaogang Wang, and Hongsheng Li. Pv-rcnn++: Point-voxel feature set abstraction with local vector representation for 3d object detection. *arXiv preprint arXiv:2102.00463*, 2021. [1, 2](#)
- [39] Shaoshuai Shi, Xiaogang Wang, and Hongsheng Li. Pointrcnn: 3d object proposal generation and detection from point cloud. In *Proceedings of the IEEE/CVF Conference on Computer Vision and Pattern Recognition*, pages 770–779, 2019. [1](#)
- [40] Shaoshuai Shi, Xiaogang Wang, and Hongsheng Li. Pointrcnn: 3d object proposal generation and detection from point cloud. In *Proceedings of the IEEE/CVF Conference on Computer Vision and Pattern Recognition (CVPR)*, June 2019. [6, 7, 8](#)
- [41] Shaoshuai Shi, Zhe Wang, Jianping Shi, Xiaogang Wang, and Hongsheng Li. From points to parts: 3d object detection from point cloud with part-aware and part-aggregation network. *IEEE transactions on pattern analysis and machine intelligence*, 2020. [1, 2](#)
- [42] OpenPCDet Development Team. Openpcdet: An open-source toolbox for 3d object detection from point clouds. <https://github.com/open-mmlab/OpenPCDet>, 2020. [2, 6, 7](#)
- [43] Sourabh Vora, Alex H Lang, Bassam Helou, and Oscar Beijbom. Pointpainting: Sequential fusion for 3d object detection. In *Proceedings of the IEEE/CVF conference on computer vision and pattern recognition*, pages 4604–4612, 2020. [2](#)
- [44] Yue Wang, Yongbin Sun, Ziwei Liu, Sanjay E Sarma, Michael M Bronstein, and Justin M Solomon. Dynamic graph cnn for learning on point clouds. *AcM Transactions On Graphics (tog)*, 38(5):1–12, 2019. [2](#)
- [45] Qiangeng Xu, Yin Zhou, Weiyue Wang, Charles R Qi, and Dragomir Anguelov. Spg: Unsupervised domain adaptation for 3d object detection via semantic point generation. In *Proceedings of the IEEE/CVF International Conference on Computer Vision*, pages 15446–15456, 2021. [1](#)
- [46] Yan Yan, Yuxing Mao, and Bo Li. Second: Sparsely embedded convolutional detection. *Sensors*, 18(10):3337, 2018. [1, 2, 6, 7, 8](#)
- [47] Zetong Yang, Yanan Sun, Shu Liu, and Jiaya Jia. 3dssd: Point-based 3d single stage object detector. In *Proceedings of the IEEE/CVF conference on computer vision and pattern recognition*, pages 11040–11048, 2020. [2](#)
- [48] Zetong Yang, Yanan Sun, Shu Liu, Xiaoyong Shen, and Jiaya Jia. Std: Sparse-to-dense 3d object detector for point cloud. In *Proceedings of the IEEE/CVF International Conference on Computer Vision*, pages 1951–1960, 2019. [2](#)
- [49] Tianwei Yin, Xingyi Zhou, and Philipp Krahenbuhl. Center-based 3d object detection and tracking. In *Proceedings of the IEEE/CVF Conference on Computer Vision and Pattern Recognition (CVPR)*, pages 11784–11793, June 2021. [2](#)
- [50] Hong Zhang. Two-dimensional optimal sensor placement. *IEEE Transactions on Systems, Man, and Cybernetics*, 25(5):781–792, 1995. [2](#)
- [51] Ji Zhang and Sanjiv Singh. Loam: Lidar odometry and mapping in real-time. In *Robotics: Science and Systems*, volume 2, 2014. [1, 2](#)
- [52] Yin Zhou and Oncel Tuzel. Voxelnet: End-to-end learning for point cloud based 3d object detection. In *Proceedings of the IEEE conference on computer vision and pattern recognition*, pages 4490–4499, 2018. [2](#)